J. Innovative Eng. Nat. Sci., vol. 5, no. 1, pp. 128-147, 2025.
http://doi.org/10.61112/jiens.1555378

JIENS
Journal of Innovative Engineering and Natural Science
(Yenilikçi Mühendislik ve Doğa Bilimleri Dergisi)
https://dergipark.org.tr/en/pub/jiens
Original Paper

Comparative assessment of element types for evaluating local elastic buckling behavior of rectangular hollow sections using finite element analysis

Mehmet Akif Dundar[a]*, Kazım Ercan[a] and Osman Özenç[a]

[a]*Yozgat Bozok University, College of Engineering, Mechanical Engineering Department, 66100, Yozgat/Turkey*

ARTICLE INFO

Article history:
Received 24 September 2024
Received in revised form 10 November 2024
Accepted 6 December 2024

Available online

Keywords:
Axial compression
Major axis bending
Minor axis bending
Local elastic buckling
Rectangular hollow sections (RHSs)
Element types
Finite element analysis

ABSTRACT

This study systematically evaluates the performance of conventional shell elements in Abaqus for predicting the local elastic buckling behavior of rectangular hollow sections (RHSs) under various loading conditions, including axial compression, major axis bending, and minor axis bending. Theoretical local buckling coefficients were first derived based on the cross-sectional dimensions of RHSs and used to calculate the critical local buckling stress for each loading scenario. Finite element analyses (FEA) were then performed using different shell element types, including four-node and eight-node elements, to assess their accuracy and computational efficiency. The results indicate that four-node shell elements (S4, S4R) offer a favorable balance of accuracy and significantly reduced computational time, making them the most efficient option. In contrast, eight-node elements (S8R, S8R5) provide marginally higher accuracy but require substantially longer computation times and have limited applicability. This study underscores the importance of selecting appropriate elements to achieve a balance between accuracy and efficiency, providing valuable guidance for engineers in structural design. By optimizing element selection for modeling local elastic buckling in RHSs, the research improves computational efficiency and supports the development of more reliable, cost-effective designs.

I. INTRODUCTION

The analysis of local buckling behavior in structural elements is a critical aspect of engineering design, especially for thin-walled structures such as rectangular hollow sections (RHSs) [1]. Local buckling significantly affects the load-bearing capacity and overall stability of these sections under various loading conditions, including axial compression and bending about both the major and minor axes [1-4]. Accurate prediction of local buckling behavior is essential to ensure the safety and performance of structures in diverse applications, ranging from civil engineering to aerospace and automotive industries. Finite element analysis (FEA) has become an indispensable tool for predicting the buckling behavior of structures [5-10]. Among the many FEA software available, Abaqus is widely recognized for its robust capabilities in handling complex structural [5, 7-17]. In Abaqus, various conventional shell element types are available, each offering different levels of computational accuracy and efficiency. These elements include the four-node shell elements S4 and S4R, and the eight-node reduced integration shell elements S8R and S8R5 [6, 18, 19].

The S4 element is a versatile four-node quadrilateral shell suitable for both thick and thin shells, capable of accommodating complex geometries, finite rotations, and membrane strains [6, 18-20]. The S4R, a reduced integration version of the S4, enhances computational efficiency and mitigates shear locking, making it ideal for large-scale models in industries such as automotive and aerospace [6, 9, 12, 19, 21]. The S4R5, using five degrees of freedom per node, accurately captures transverse shear deformation, benefiting thick-walled structures [19, 22,

*Corresponding author. Tel.: +90-544-463-4075; e-mail: m.akif.dundar@yobu.edu.tr

23]. The S8R, an eight-node quadrilateral shell with reduced integration, provides higher-order interpolation for accurately modeling curved geometries and high deformation gradients [19, 24-26]. The S8R5 combines this higher-order interpolation to better capture transverse shear effects, making it suitable for detailed analyses of thick shell structures [6, 7, 19, 27, 28]. These elements are selected based on a balance of computational efficiency and accuracy to meet specific simulation needs. Among the aforementioned conventional shell elements, only the S4 uses full integration; others employ reduced integration [19]. The S4, S4R, and S4R5 elements use linear interpolation, while the S8R and S8R5 elements employ quadratic shape functions. S4 and S4R are four-node, doubly-curved shells with six degrees of freedom per node (three translational and three rotational) [19]. The S4R5, also four-node, has five degrees of freedom (three translational and two in-plane rotational). The eight-node S8R uses reduced integration with six degrees of freedom per node, suitable for higher-order interpolation. The S8R5, another eight-node element, combines higher-order interpolation with five degrees of freedom per node, enhancing transverse shear effect modeling for thin shells [19].

The aforementioned element types have been widely employed by researchers in finite element analyses of local buckling behavior of structural members typically subjected to axial compression [6, 18, 21, 24, 28–37]. The literature review revealed that the S4 and S4R elements are more commonly used in local buckling simulations. Their frequent use can be attributed to their optimal balance between computational efficiency and accuracy, making them highly suitable for diverse structural analysis applications [2, 3, 18, 21, 28, 31–33, 35, 38]. These elements apply thick shell theory when the shell thickness increases and transition to discrete Kirchhoff thin shell elements as the thickness decreases. A significant advantage of these two element types is their ability to account for variations in shell thickness [6]. However, studies have indicated that the S4 element, while achieving superior numerical convergence, demands more computational time compared to the S4R element [6]. Conversely, research has indicated that the S4R element yields results comparable to the S4 element but requires significantly less computational time. This difference in processing time is especially notable for large local buckling models, where memory requirements are a critical concern [18]. Additionally, studies have reported that the S4R5 element is not well-suited for finite strain problems [35]. A study reported that the S8R element, intended for thick shells with a thickness greater than 1/15 of the characteristic length, supports large arbitrary rotations but only small strains and ignores deformation in the thickness direction [6]. Moreover, the S8R5 element, although suitable for thin shells, can produce inaccurate buckling results due to the potential misalignment of the internally defined center node with the actual shell surface [6]. Additionally, these element types require significantly longer computational times, which further limits their practicality in certain applications.

Despite the availability of various shell elements, comprehensive studies comparing their performance specifically in the context of local elastic buckling of RHS under different loading conditions are lacking. Such a comparative study is crucial to understand the trade-offs between computational efficiency and accuracy, guiding engineers and researchers in selecting the most appropriate element types for their applications.

Thus, this study aims to evaluate the computational accuracy and efficiency of the aforementioned conventional shell element types in Abaqus for modeling the local elastic buckling behavior of RHS under axial compression, major axis bending, and minor axis bending. By conducting detailed simulations and comparing the results with theoretical predictions, this study endeavors to identify the most suitable element types for accurate and efficient simulation of local elastic buckling phenomena. The outcomes of this research will provide valuable insights for

the engineering community, aiding in the optimization of structural designs and contributing to the advancement of computational mechanics.

II. THEORETICAL BACKGROUND AND CALCULATIONS

1. Theory

The critical local elastic buckling stress (σ_{cr}) for box sections under any type of loading can be determined using the well-known formula written below [1, 5, 38-40].

$$\sigma_{cr} = k_\sigma \frac{\pi^2 E}{12(1-v^2)} \left(\frac{t}{d}\right)^2 \tag{1}$$

where k_σ is the local elastic buckling coefficient and E is the elastic modulus. v represents the Poisson's ratio. d is the width or height of the relevant wall segment of a box section and t denotes the thickness of the relevant wall segment.

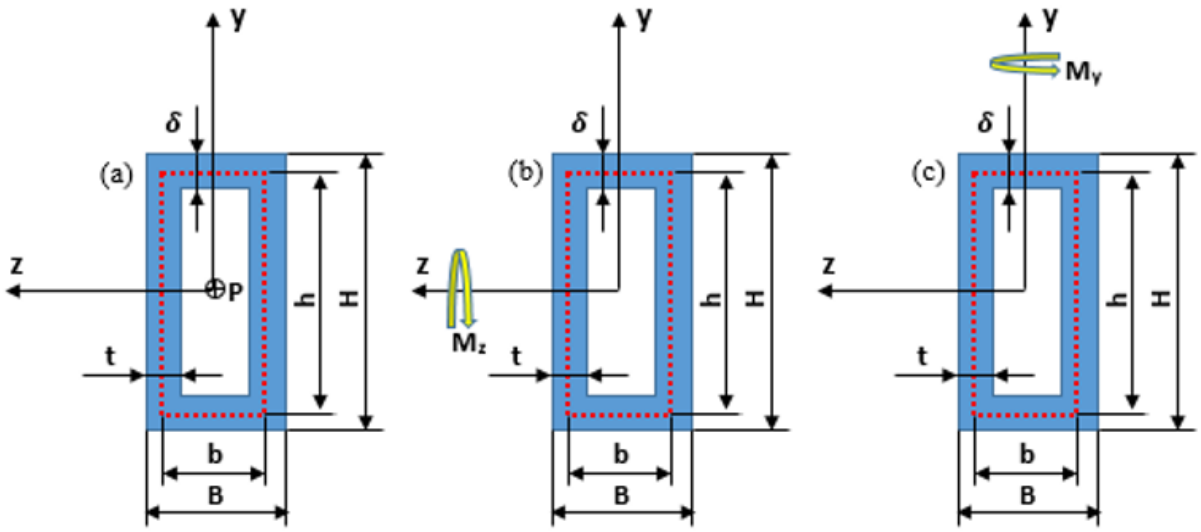

Figure 1. A cross-section of RHS under various loads, (a) Axial compression (P), (b) Major axis bending (M_z) and (c) Minor axis bending (M_y)

Eq. (1) can be rearranged for the RHS depicted in Figure 1, as follows:

$$\sigma_{cr} = k_w \frac{\pi^2 E}{12(1-v^2)} \left(\frac{t}{h}\right)^2 = k_f \frac{\pi^2 E}{12(1-v^2)} \left(\frac{\delta}{b}\right)^2 \tag{2}$$

where k_w and k_f are the local elastic buckling coefficients for the web and flange segments of the section, respectively. t and δ represent the thickness of the web and flange segments, respectively. b and h are the mid-

line width and mid-line height of the section, respectively. These two parameters (b and h) can be identified as given below.

$$b = B - t \text{ and } h = H - \delta \tag{3}$$

where H is the height of the RHS and B is the width, as demonstrated in Figure 1. Solving the equality given in Eq. (2) yields the following expression, which relates the local elastic buckling coefficient of the flange segment to that of the web segment [39, 41].

$$k_f = k_w \left(\frac{b}{h}\right)^2 \left(\frac{t}{\delta}\right)^2 \tag{4}$$

When $t = \delta$, Eq. (4) further reduces to

$$k_f = k_w \left(\frac{b}{h}\right)^2 \tag{5}$$

Eq. (2) is rearranged to highlight its simplification as follows:

$$\sigma_{cr} = k_w . n . \left(\frac{t}{h}\right)^2 \text{ or } \sigma_{cr} = k_f . n . \left(\frac{\delta}{b}\right)^2 \tag{6}$$

Here, n is the notation and represents $n = \frac{\pi^2 E}{12(1-\nu^2)}$.

The local elastic buckling coefficients, k_w and k_f, are essential in determining the critical local elastic buckling stress. The accuracy of σ_{cr} is heavily dependent on the precise value of the relevant coefficients, highlighting the necessity of a thorough understanding of this parameter. Despite its importance, limited studies [39–41] specifically address the determination of the buckling coefficients, which is affected by boundary conditions, the main dimensions of the box section, and loading types, such as axial compression, major axis bending, minor axis bending, and biaxial bending.

A noteworthy study developed an analytical expression for calculating the local elastic buckling coefficient of a box section under axial compression (Figure 1a) with simply supported boundary conditions [40]. This study introduced two specific buckling coefficients: k_w for the web segment and k_f for the flange segment, both critical for accurately predicting the local buckling behavior.

The local elastic buckling coefficient for the flange segment of the RHS subjected to axial compression (Figure 1a) can be calculated using the following expression [40].

$$k_f = \frac{4}{\left(h/b\right)^{1.7}} \tag{7}$$

Similarly, the local elastic buckling coefficient for the web segment of the RHS under major axis bending (Figure 1b) can be calculated using the following formula [40].

$$\frac{1}{k_w} = \frac{0.19}{(h/b)^3} + 0.03 \tag{8}$$

Furthermore, the local elastic buckling coefficient for the flange segment of the RHS under minor axis bending (Figure 1c) can be specified using the following expression [40].

$$k_f = \frac{5.5}{(h/b)^2} \tag{9}$$

Emphasizing here, the formulas presented in Eqs. (7) – (9), are applicable exclusively to box sections possessing equal wall segment thicknesses [2, 5, 38–40]. Given Eq. (5), knowing one of the relevant buckling coefficients implies that the other is also known.

The critical local elastic buckling load of axially compressed RHS can be determined using the formula written below [40].

$$P_{cr} = \sigma_{cr} \,.\, A_g \tag{10}$$

where A_g is the gross cross-sectional area of the RHS and can be calculated as follows:

$$A_g = H\ x\ B - (H - 2\delta)\ (B - 2t) \tag{11}$$

The critical local elastic moment of the RHS under major axis bending can also be determined by the expression given below [40].

$$M_{cr,major} = \sigma_{cr} \,.\, w_z \tag{12}$$

Herein, w_z is the section modulus of the RHS about the z- axis (strong axis), illustrated in (Figure 1b), and can be determined as follows [38, 40]:

$$w_z = \frac{BH^2}{6}\left[1-\left(1-\frac{2t}{B}\right)\left(1-\frac{2\delta}{H}\right)^3\right] \quad (13)$$

In the same manner, the critical local elastic moment of the RHS under minor axis bending can be computed using the expression given below [2, 38, 40].

$$M_{cr\_minor} = \sigma_{cr} \, . w_y \quad (14)$$

where w_y is the section modulus about the y-axis (weak axis), depicted in Figure 1c, and can be defined by [38]:

$$w_y = \frac{HB^2}{6}\left[1-\left(1-\frac{2\delta}{H}\right)\left(1-\frac{2t}{B}\right)^3\right] \quad (15)$$

2. Calculations of the Critical Local Elastic Buckling Loads for RHS

This section addresses the determination of critical local buckling loads for axial compression, major axis bending, and minor axis bending of RHS with the geometric specifications documented in Table 1.

Table 1. The geometric specifications of the RHS addressed

Specimen	**b** *(mm)*	**h** *(mm)*	**t** = **δ** *(mm)*	**L** *(mm)*
RHS-20 x 40 x 1	20	40	1	200

Note that L in Table 1 represents the length of the RHS profile. Additionally, the RHS addressed in this study is assumed to be fabricated from S235 steel grade, with the corresponding material properties detailed in Table 2 [42].

Table 2. Material properties of S235 steel grade [42]

Material	***E*** *(GPa)*	***v***	σ_y *(GPa)*	σ_u *(GPa)*
S235	210	0.3	0.282	0.324

In Table 2, σ_y and σ_u denote the yield strength and ultimate strength of the RHS material, respectively.

Procedure for calculating critical local elastic buckling loads of the RHS under axial compression, major axis bending, and minor axis bending is as follows:

- Determine local elastic buckling coefficients:
  - *For the flange segment: k_f using Eq. (7) for axial compression, Eq. (5) for major axis bending, and Eq. (9) for minor axis bending.*
  - *For the web segment: k_w using Eq. (5) for axial compression, Eq. (8) for major axis bending, and Eq. (5) for minor axis bending.*
- Calculate the parameter n using material properties from Table 2 for all loading conditions.
- Calculate critical local elastic stress using Eq. (6) for all cases.

- Determine additional parameters:
  - *Gross cross-sectional area using Eq. (11) for axial compression.*
  - *Section modulus about the z-axis (w_z) using Eq. (13) for major axis bending.*
  - *Section modulus about the y-axis (w_y) using Eq. (15) for minor axis bending.*
- Calculate critical local elastic buckling loads/moments:
  - *Using Eq. (10) for axial compression.*
  - *Using Eq. (12) for major axis bending.*
  - *Using Eq. (14) for minor axis bending.*

Upon completing the outlined calculation steps, the results for the RHS subjected to axial compression, major axis bending, and minor axis bending are presented in Tables 3, 4, and 5, respectively.

Table 3. The critical local elastic buckling stress and corresponding bifurcation load of RHS under axial compression

Loading Type	k_f	k_w	n *(GPa)*	σ_{cr} *(GPa)*	A_g *(mm²)*	P_{cr} *(kN)*
Axial Compression	1.231	4.924	189.8	0.584	120	70.08

Table 4. The critical local elastic buckling stress and corresponding bifurcation moment of the RHS under major axis bending

Loading Type	k_f	k_w	n *(GPa)*	σ_{cr} *(GPa)*	w_z *(mm³)*	M_{cr_major} *(kN.mm)*
Major Axis Bending	4.651	18.604	189.8	2.207	1302	2873.5

Table 5. The critical local elastic buckling stress and corresponding bifurcation moment of the RHS under minor axis bending

Loading Type	k_f	k_w	n *(GPa)*	σ_{cr} *(GPa)*	w_y *(mm³)*	M_{cr_minor} *(kN.mm)*
Minor Axis Bending	1.375	5.5	189.8	0.652	890.5	580.6

In essence, the critical local elastic buckling stresses and corresponding bifurcation loads of the RHS subjected to various types of loading, including axial compression, major axis bending, and minor axis bending, have been theoretically determined. The analytical expressions and procedures presented in this study can also be applied to determine the critical local elastic buckling stresses of RHSs with different *h/b* ratios under the aforementioned loading conditions.

III. FINITE ELEMENT PROCEDURE

To investigate the influence of different element types on the local elastic buckling behavior of rectangular hollow sections (RHS) under various loading conditions, a linear elastic eigenvalue buckling analysis was conducted. The RHS model was discretized using five distinct shell elements: S4, S4R, S4R5, S8R, and S8R5. This comprehensive analysis is crucial for understanding how each element type affects the accuracy and computational efficiency of predicting buckling behavior. By comparing these shell elements, the study aims to provide insights that will guide the selection of the most appropriate element type for various engineering applications, ensuring optimal performance and reliability in structural analysis and design.

In Abaqus, various conventional shell element types are designed to meet different modeling requirements with distinct advantages. The S4 is a four-node, doubly curved general-purpose shell element capable of handling finite membrane strains [6, 43-45]. This element type is versatile and suitable for complex geometries, providing reliable

results for both thick and thin shell applications. The S4R is a similar four-node element but features reduced integration with hourglass control, enhancing computational efficiency while also accommodating finite membrane strains [2, 8, 38, 44]. The reduced integration helps mitigate shear locking, making S4R ideal for large-scale models in industries such as automotive and aerospace. The S4R5, another four-node element, is optimized for thin shell applications, incorporating reduced integration, hourglass control, and five degrees of freedom per node to accurately capture transverse shear deformations [35, 37, 44, 45]. This makes the S4R5 particularly useful for detailed analyses of thick-walled structures.

The S8R is an eight-node, doubly curved thick shell element that employs reduced integration, making it suitable for thick shell applications [6, 26, 44]. It supports large arbitrary rotations but only small strains, and it ignores deformation in the thickness direction. Despite providing accurate results in specific scenarios, its applicability can be limited due to these characteristics. The S8R5, an eight-node thin shell element with reduced integration and five degrees of freedom per node, improves the accuracy of transverse shear effects. However, the potential misalignment of the internally defined center node with the actual shell surface can lead to inaccurate buckling results, particularly in thin shell applications [44, 46, 47].

Each element type offers a balance between computational efficiency and precision tailored to the specific needs of various simulations. The choice of element type is critical in ensuring the optimal performance of finite element models, particularly in large-scale or computationally intensive analyses. This study highlights the importance of understanding the strengths and limitations of each shell element type to make informed decisions in structural analysis and design.

Figure 2 illustrates the finite element models of the RHS, including loading and boundary conditions, as well as mesh configurations: Figure 2a presents the model for axial compression, while Figure 2b and Figure 2c depict the models for major axis bending and minor axis bending, respectively. Three distinct finite element models were developed for these loading cases. Reference points were established at the midpoints of both ends of the RHS and connected to the sections using kinematic couplings for axial compression and rigid body-pin constraints for major and minor axis bending, as per the methodologies described in [38, 48]. Separate simulations were conducted for each loading scenario to ensure accurate representation and validation of the finite element analysis. Kinematic couplings were used for axial compression because they allow the load to be uniformly distributed across the cross-section, ensuring a realistic simulation of axial load transmission. They are particularly useful for transmitting forces and moments to a structure without inducing artificial constraints that could alter the structural response [19]. On the other side of the coin, in major axis bending and minor axis bending simulations, rigid body constraints with pin nodes were deployed to enforce a rigid connection between the reference node and the nodes on the surface, allowing for rotational and translational movements relative to a specified point. This setup is beneficial for bending simulations because it accurately represents the boundary conditions where moments are applied, ensuring the load is correctly transmitted to induce bending about the desired [19].

For axial compression, a unit load was applied and transmitted to the RHS. In the cases of major axis and minor axis bending, a unit moment was applied to achieve the desired deformation. This setup ensures a comprehensive evaluation of the local buckling behavior under different loading conditions, thereby validating the accuracy and reliability of the finite element analysis. The detailed configurations and application of loads and constraints in the

models allow for precise simulation and insightful comparisons of the performance of various shell element types in Abaqus.

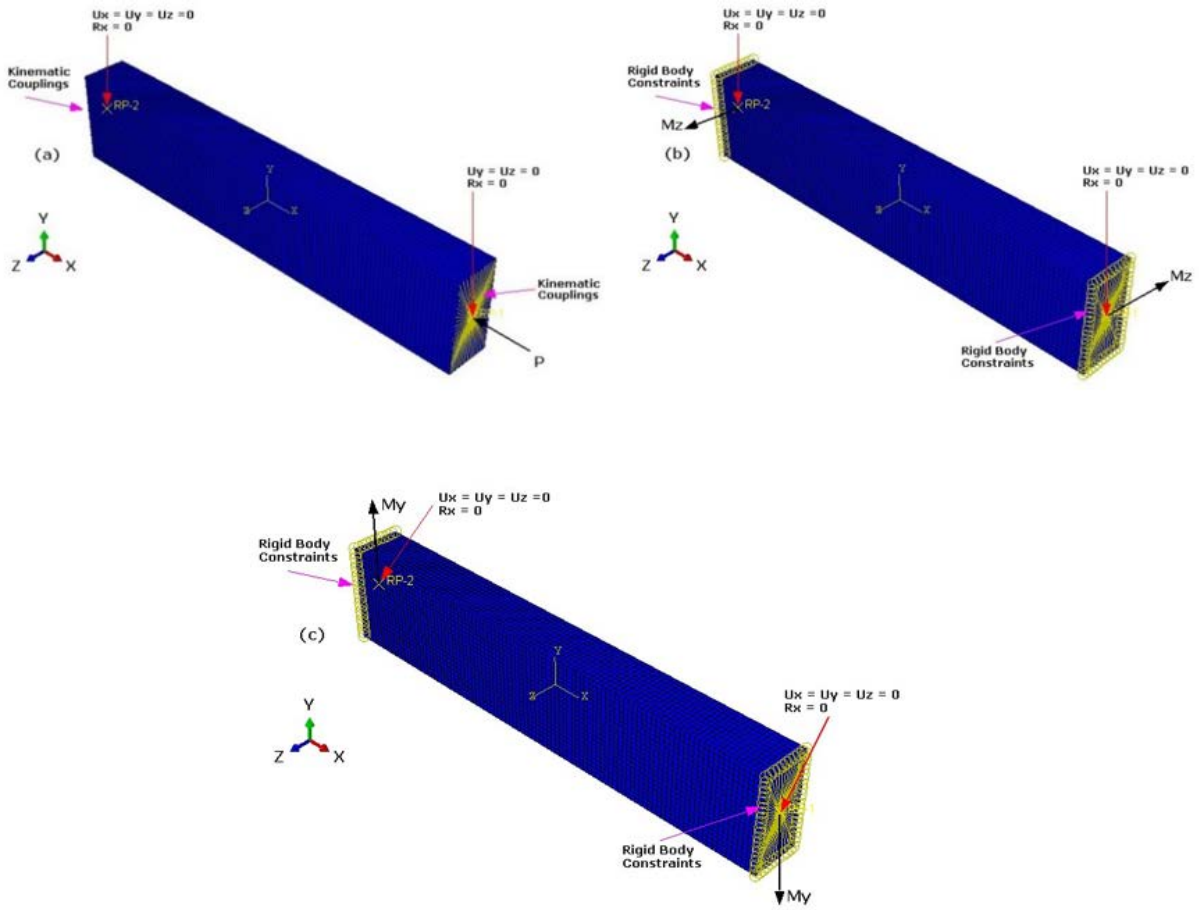

Figure 2. The finite element model of RHS under various loads, (a) Axial compression (P), (b) Major axis bending (M_z), and (c) Minor axis bending (M_y)

The elastic material properties, including the elastic modulus and Poisson's ratio documented in Table 2, were utilized in the simulations. The subspace iteration eigen-solver method was employed, with the number of vectors per iteration set to five. To ensure the accuracy and reliability of the finite element procedure, a mesh convergence analysis was conducted on the RHS under axial compression. The mesh was progressively refined until the results stabilized, demonstrating the model's consistency. As shown in Figure 3, convergence was achieved when the element size was reduced below 5 mm. Consequently, a mesh size of 2 mm was chosen for the entire RHS based on the mesh convergence study results. A total of 600 elements and 6060 nodes were used in the simulations, with each element meshed into a square shape (aspect ratio of 1) to enhance accuracy [2]. The choice of mesh size is crucial in buckling simulations as it directly impacts the accuracy and precision of the predicted buckling behavior [49-54].

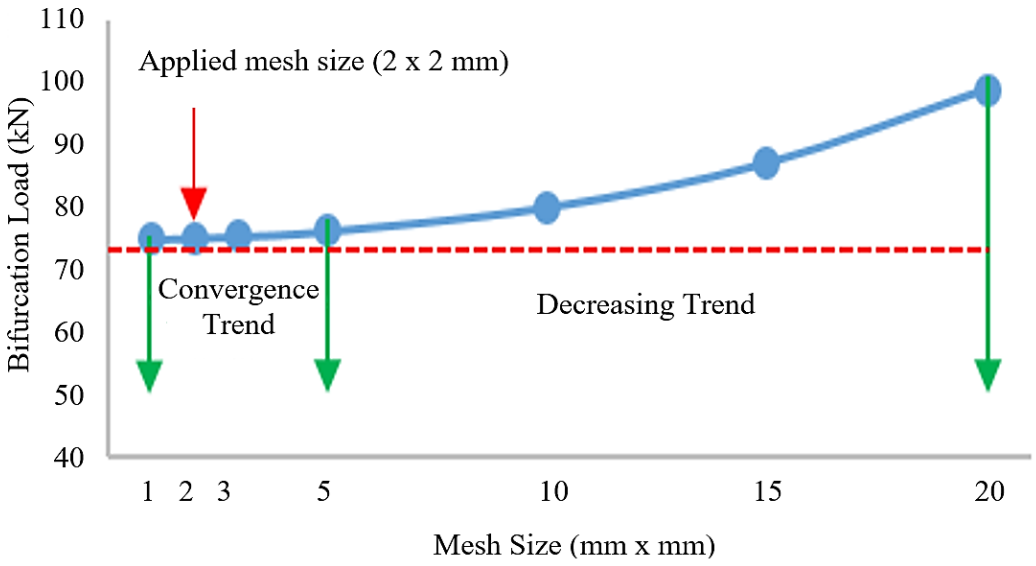

Figure 3. Results of the mesh convergence study

IV. RESULTS AND DISCUSSIONS

The local buckling modes and corresponding bifurcation loads of the axially compressed RHS, extracted from the linear elastic eigenvalue buckling analyses, are depicted in Figure 4. The local elastic buckling mode shapes estimated for the RHS under axial compression, as shown in Figure 4, are consistent with those reported in the relevant literature [2, 38, 39]. While the mode shapes are largely unaffected by the element type employed in the analysis, the critical local elastic buckling loads exhibit varying degrees of sensitivity to the element type. These discrepancies are particularly notable when compared to theoretical results, as reported in Table 6 and graphically illustrated in Figure 5. This sensitivity underscores the importance of selecting the appropriate element type in finite element analyses to ensure accurate predictions of buckling loads. Different element formulations can influence the precision of the computed buckling loads, highlighting the need for careful consideration in element selection to achieve reliable and accurate structural analysis outcomes.

Table 6. Comparison of element types for critical local elastic buckling load of RHS under axial compression

Element Type	Bifurcation Load P_{cr} *(kN)*		Wall-clock Time *(Sec)*	|Error| *%*
	FEM	Theory		
S4	74.88	70.08	24	6.971
S4R	74.918	70.08	21	7.025
S4R5	75.067	70.08	27	7.238
S8R	74.688	70.08	90	6.697
S8R5	74.408	70.08	116	6.297

Drawing from the findings in Figure 5 and Table 6, the evaluation of various element types for estimating the critical local elastic buckling load of an RHS under axial compression yields insightful conclusions. The S4 element achieves a bifurcation load of 74.88 kN with an error of 6.971%, balancing accuracy and computational efficiency with a wall-clock time of only 24 seconds. The S4R element, slightly less accurate with an error of 7.025%, offers enhanced efficiency, completing the analysis in 21 seconds. In contrast, the S4R5 element, with

five degrees of freedom per node, exhibits the highest error among the 4-node elements at 7.238%, requiring 27 seconds of computation.

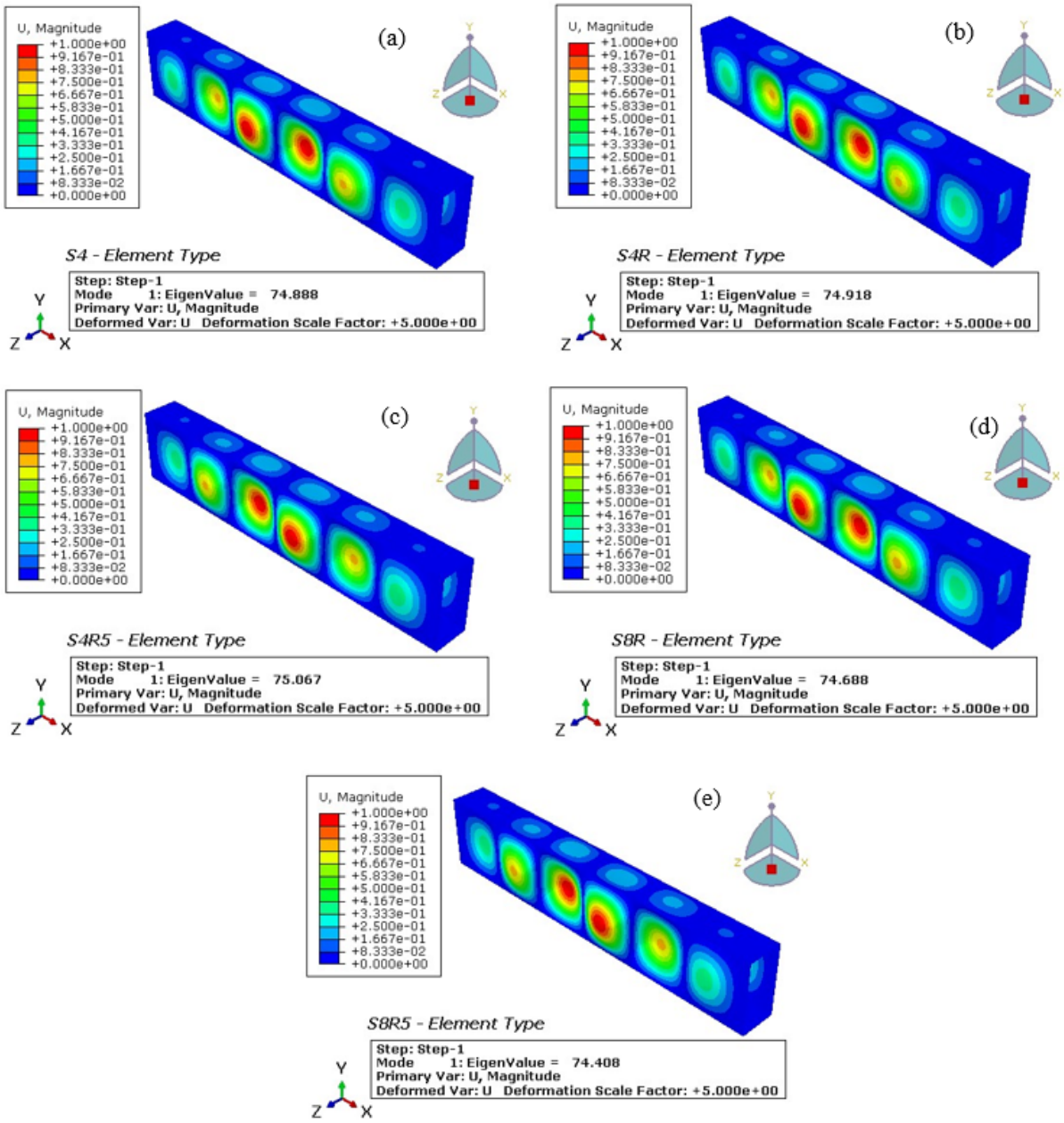

Figure 4. Local elastic buckling modes and corresponding bifurcation loads predicted for the axially compressed RHS by using various element types, (a) S4, (b) S4R, (c) S4R5, (d) S8R, and (e) S8R5

The S8R element yields the second-lowest error at 6.697% but demands significantly more computational time at 90 seconds, making it suitable for accuracy-critical applications. The S8R5 element, despite providing the highest accuracy with an error of 6.297%, incurs the greatest computational expense at 116 seconds, positioning it as the preferred choice for precise analyses. Overall, the S4R element is recommended for routine applications where computational efficiency is paramount, whereas the S8R5 element is ideal for high-precision tasks, despite its increased computational demands.

The discrepancies observed between element types can be attributed to their respective formulations and integration schemes. For instance, the reduced integration in S4R, S4R5, S8R, and S8R5 elements enhances computational efficiency but can introduce numerical inaccuracies, especially in complex buckling scenarios. Conversely, the full integration used in S4 elements improves accuracy but at the cost of higher computational resources. This analysis underscores the essential trade-off between computational efficiency and accuracy, enabling informed selection of element types based on specific analysis requirements and resource constraints.

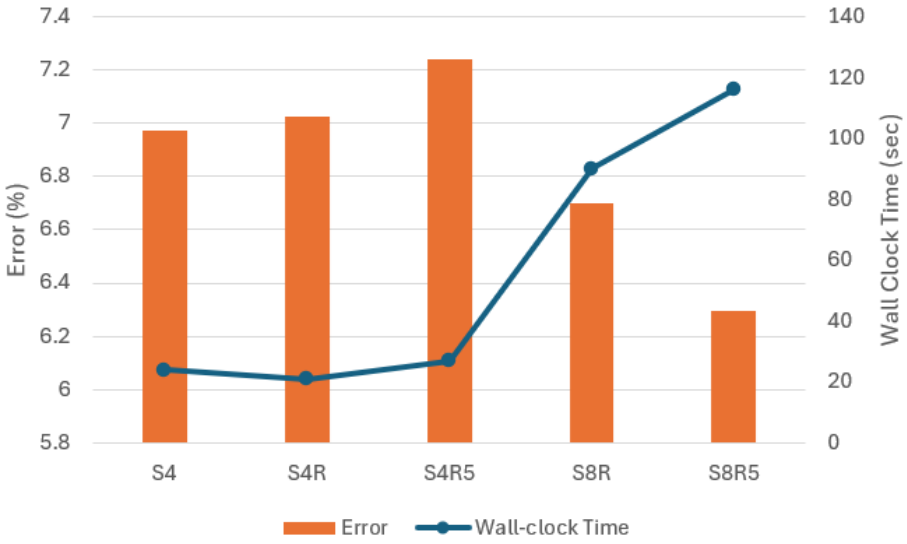

Figure 5. Error and analysis time comparison of element types for critical local elastic buckling load of RHS under axial compression

In this case, since the structure is considered thin (with thickness less than about 1/15 of a characteristic length on the surface of the shell), the S4, S4R, S4R5, S8R, and S8R5 elements are evaluated accordingly. The S4 and S4R elements are 4-node quadrilateral shell elements. S4 employs full integration for high accuracy but at a higher computational cost, while S4R uses reduced integration for enhanced efficiency but with potential numerical issues. The S4R5 element, also using reduced integration with five degrees of freedom per node, is optimized for thin shells but can compromise accuracy in some scenarios.

The S8R element, designed for thick shells, is less suitable here despite its second-lowest error due to its higher computational demands. The S8R5 element, however, provides high accuracy for thin shells with its five degrees of freedom per node and reduced integration, making it the best choice for precision despite its computational expense.

In conclusion, for thin structures, the S4R element offers a good balance of efficiency and accuracy for routine applications, while the S8R5 element is recommended for tasks requiring high precision, despite the increased computational requirements.

The local elastic buckling mode shapes identified for the RHS under major axis bending, as illustrated in Figure 6, were found to be consistent with those reported in the relevant literature [2, 38, 39]. Although the mode shapes were basically unaffected by the choice of element type in the analysis, the critical local elastic buckling loads

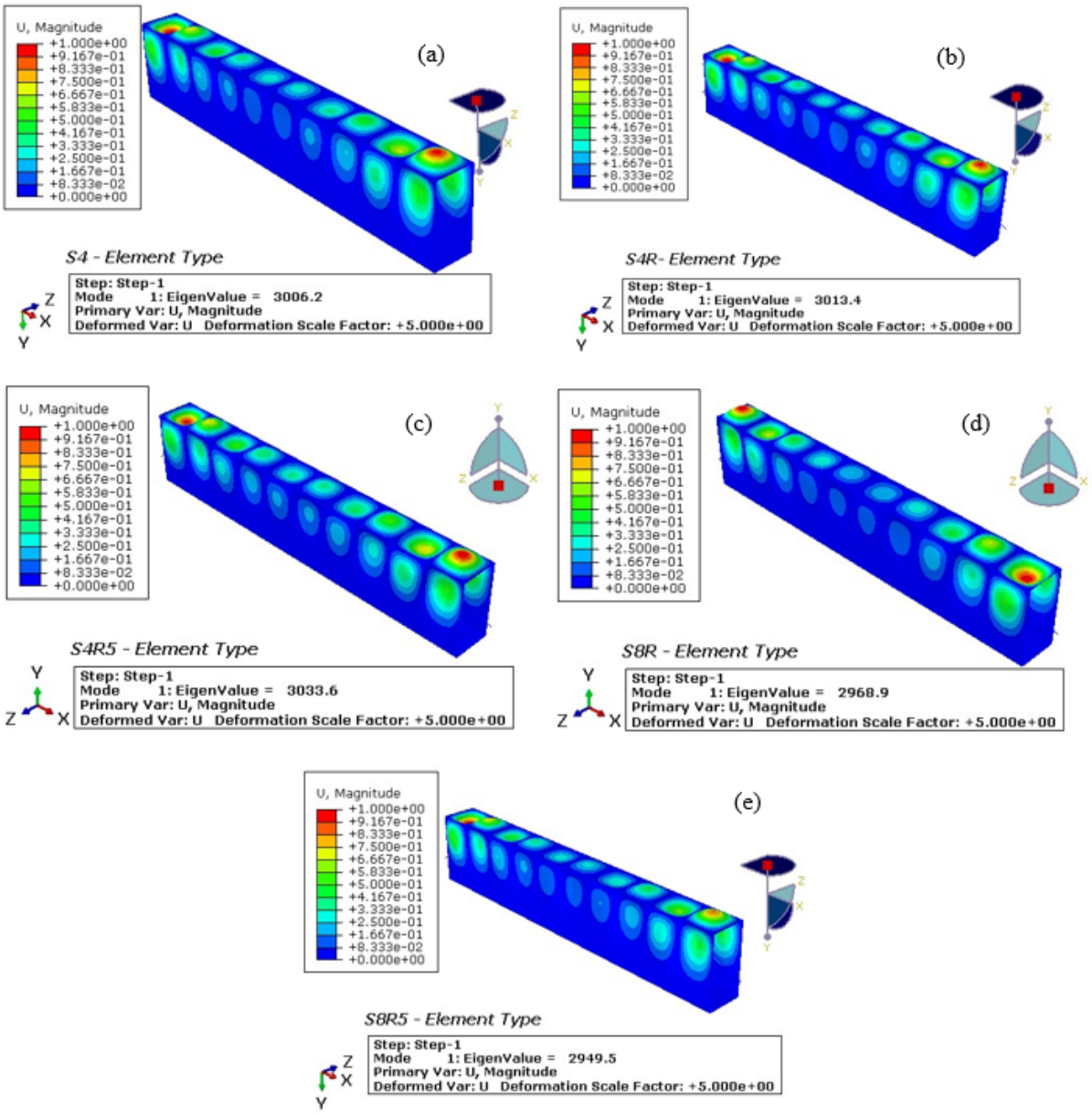

Figure 6. Local elastic buckling modes and corresponding bifurcation moments predicted for the RHS under major axis bending by using various element types, (a) S4, (b) S4R, (c) S4R, (d) S8R, and (e) S8R5

exhibited varying sensitivities to the element types, reflecting differences when compared to the theoretical results, as documented in Table 7 and shown in Figure 7. The results of major axis bending reported in Table 7 and Figure 7 indicate that the error ratios are generally lower compared to those observed in axial compression, highlighting the superior accuracy of the analyzed element types in this loading condition. Specifically, the S8R5 element demonstrates the highest accuracy with an error of 2.644%, followed closely by S8R at 3.319%, reflecting their effective formulation for capturing thin shell behavior due to reduced integration techniques. In contrast, while the S4R5 and S4R elements exhibit slightly higher error rates of 5.571% and 4.868%, respectively, they maintain competitive computational times, emphasizing their balance between efficiency and accuracy. Notably, the wall-clock times for major axis bending are significantly higher, with S8R5 taking 870 seconds, compared to axial compression simulations. This can be attributed to the increased complexity in capturing the bending responses

and deformation patterns, which necessitate more extensive computational resources. Overall, these findings suggest that while the element formulations effectively capture local buckling phenomena, the choice of element type significantly influences both the accuracy and computational demands, underscoring the importance of selecting appropriate models based on the specific loading conditions and structural behavior.

Table 7. Comparison of element types for critical local elastic buckling moment of RHS under major axis bending

Element Type	**Bifurcation Moment** M_{cr_major} *(kN.mm)*		**Wall-clock Time** *(Sec)*	**|Error|** *%*
	FEM	**Theory**		
S4	3006.2	2873.5	155	4.618
S4R	3013.4	2873.5	151	4.868
S4R5	3033.6	2873.5	140	5.571
S8R	2968.9	2873.5	447	3.319
S8R5	2949.5	2873.5	870	2.644

Figure 7. Error and analysis time comparison of element types for critical local elastic buckling load of RHS under major axis bending

The error ratios between the element types indicate negligible differences, with the S4 and S4R elements exhibiting an error difference of only 0.25% (4.618% for S4 vs. 4.868% for S4R), making them practically equivalent. In contrast, the S4 and S8R5 elements show a more significant error difference of 2.973% (4.618% for S4 vs. 2.644% for S8R5), highlighting the superior accuracy of the S8R5 element. Given these findings, it is recommended that for applications prioritizing computational efficiency, the S4 or S4R elements be utilized due to their reasonable accuracy and lower computational demands. Conversely, for analyses requiring high precision in major axis bending, the S8R5 element is advisable despite its increased computational time. This approach facilitates a balanced selection of element types based on the specific accuracy and efficiency needs of the project.

The local elastic buckling modes and corresponding bifurcation moments predicted for the RHS under minor axis bending using various element types are illustrated in Figure 8. The results presented in Table 8, as well as graphically presented in Figure 9, underscore the significance of evaluating different element types in determining the critical local elastic buckling moment of RHS under minor axis bending, highlighting considerations of accuracy, computational efficiency, and the inherent trade-offs among various element types. Notably, the local

elastic buckling modes identified in this study are consistent with existing literature, reinforcing the validity of the findings.

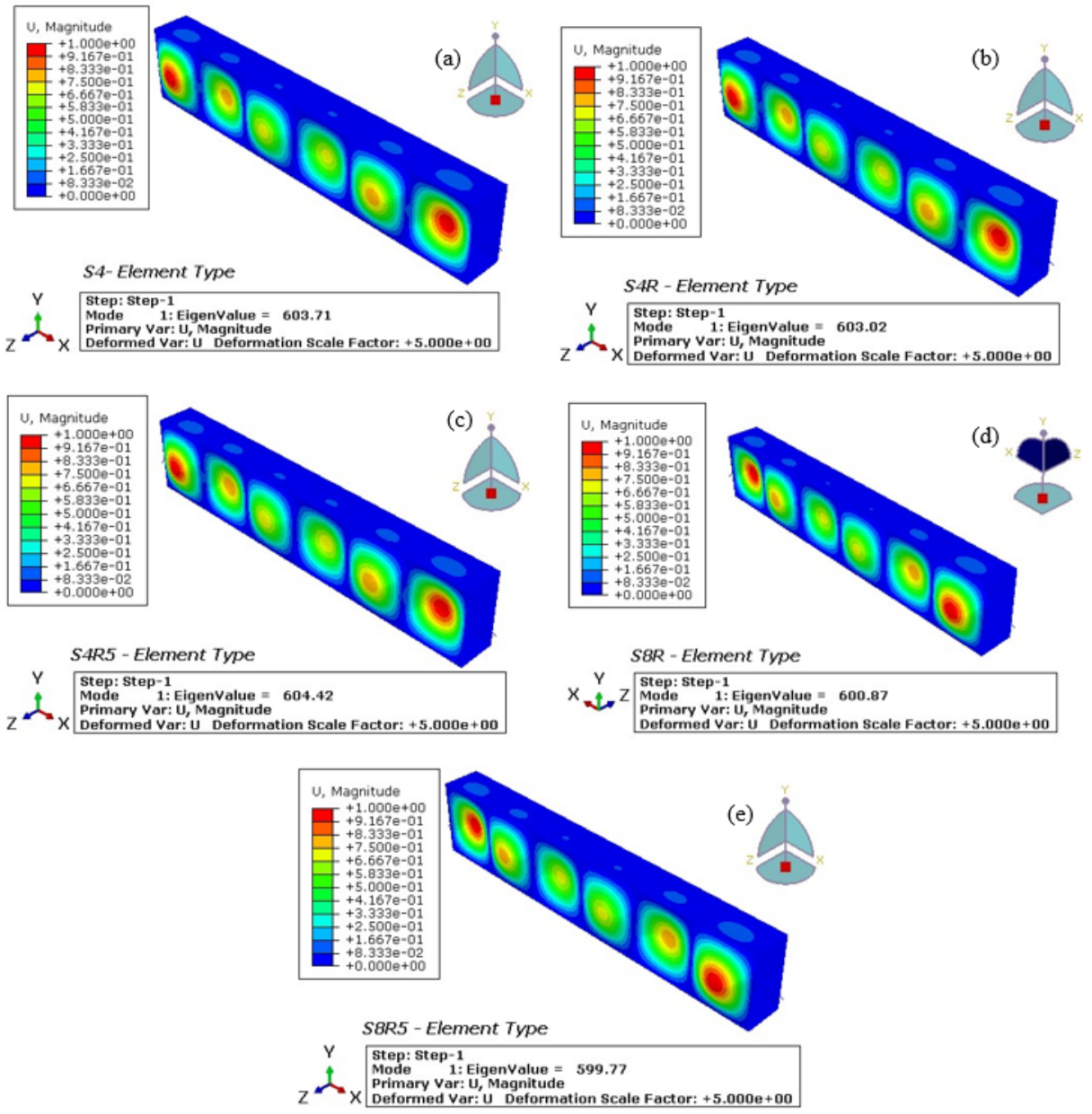

Figure 8. Local elastic buckling modes and corresponding bifurcation moments predicted for the RHS under minor axis bending by using various element types, (a) S4, (b) S4R, (c) S4R5, (d) S8R, and (e) S8R5

Table 8. Comparison of element types for critical local elastic buckling moment of RHS under minor axis bending

Element Type	**Bifurcation Moment** $M_{cr\ minor}$ *(kN.mm)*		**Wall-clock Time** *(Sec)*	**|Error|** *%*
	FEM	**Theory**		
S4	603.71	580.6	54	3.981
S4R	603.02	580.6	53	3.861
S4R5	604.42	580.6	46	4.102
S8R	600.87	580.6	221	3.491
S8R5	599.77	580.6	305	3.301

The S4 element yields a bifurcation moment of 603.71 kN.mm, accompanied by an error of 3.981%, reflecting a commendable balance between accuracy and computational efficiency, with a computation time of 54 seconds. Similarly, the S4R element achieves a moment of 603.02 kN.mm, demonstrating a marginally lower error of 3.861% and a computation duration of 53 seconds. In contrast, the S4R5 element presents a higher error of 4.102%, resulting in a moment of 604.42 kN.mm while requiring 46 seconds for analysis. Among the eight-node element types, the S8R element produces a bifurcation moment of 600.87 kN.mm with an error of 3.491%, although it demands significantly greater computational time, totaling 221 seconds. The S8R5 element, while yielding a slightly lower moment of 599.77 kN.mm, achieves the highest accuracy with an error of 3.301%, albeit with an extended computation duration of 305 seconds.

In summary, the S4 and S4R elements are recommended for scenarios prioritizing computational efficiency, whereas the S8R5 element is more suited for high-precision analyses, notwithstanding its longer computation time. The evaluations across axial compression, major axis bending, and minor axis bending reveal distinct performance characteristics among the element types. For axial compression, the S4 and S4R elements demonstrate a satisfactory balance between accuracy and computational efficiency, exhibiting errors of approximately 7% with computation times of 24 and 21 seconds, respectively. Conversely, the S8R and S8R5 elements provide higher accuracy but necessitate substantially greater computational times.

In major axis bending, the S4 and S4R elements maintain their efficiency, with errors around 4.6% and 4.8% and computation times of 155 and 151 seconds, respectively. The S8R5 element, while delivering the highest accuracy, incurs increased computation time. For minor axis bending, the S4 and S4R elements again exhibit efficient performance, with errors below 4%, while the S8R5 element offers the highest accuracy, requiring the longest computation time of 305 seconds.

Overall, the S4 and S4R elements are recommended for applications that prioritize computational efficiency, while the S8R5 element is ideal for high-precision analyses. Although the S8R and S8R5 elements demonstrate commendable accuracy -with error ratios of 6.697% and 6.297%, respectively, under axial compression, 3.319% and 2.644% under major axis bending, and 3.491% and 3.301% under minor axis bending- their reliability is not universal. The S8R element, designed for thick shells, neglects deformation in the thickness direction, which is critical for thin plates [6, 44]. Conversely, the S8R5 element, tailored for thin shells, may yield inaccuracies in buckling problems due to potential misalignment of its internally defined center node with the actual shell surface [6, 44].

Both the S4 and S4R elements exhibit comparable accuracy across all loading conditions: axial compression, major axis bending, and minor axis bending. The S4 element records slightly lower error percentages for axial compression (6.971% vs. 7.025%) and major axis bending (4.618% vs. 4.868%), while the S4R element shows a marginally lower error for minor axis bending (3.861% vs. 3.981%). In terms of computational efficiency, the S4R element consistently requires less time: 21 seconds compared to 24 seconds for axial compression, 151 seconds compared to 155 seconds for major axis bending, and 53 seconds compared to 54 seconds for minor axis bending. Based on these findings, the S4R element is recommended for applications emphasizing computational efficiency, while the S4 element remains a viable choice for scenarios where slightly higher accuracy is desired.

Nonetheless, the differences in error percentages between the S4 and S4R elements are minimal across all loading conditions. The slight increase in error associated with the S4R element is offset by its significant reduction in

computational time, establishing the S4R element as a more appropriate choice for large-scale analyses or scenarios where time efficiency is paramount. Consequently, the S4R element is advocated for its effective performance, achieving a favorable balance between computational efficiency and accuracy.

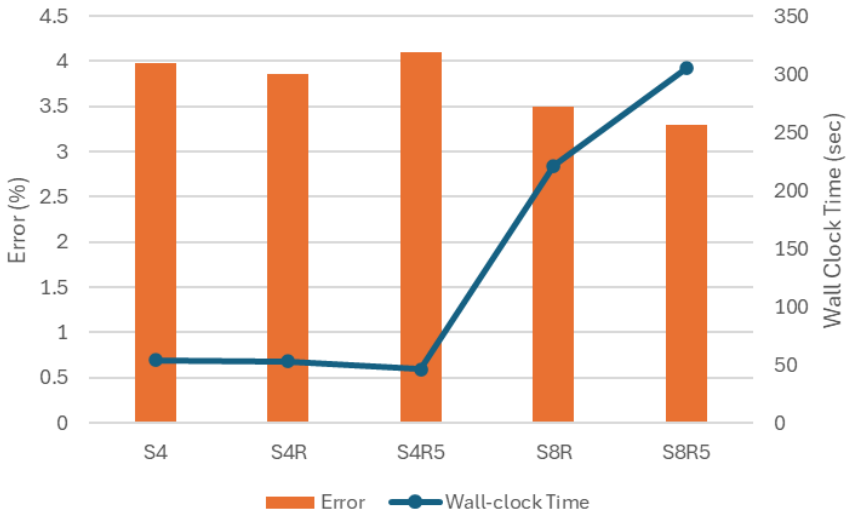

Figure 9. Error and analysis time comparison of element types for critical local elastic buckling load of RHS under minor axis bending

V. CONCLUDING REMARKS

The following conclusions can be drawn from the findings of the study.

- The S4 element achieves a balanced performance with low error percentages of 6.971% for axial compression, 4.618% for major axis bending, and 3.981% for minor axis bending, requiring moderate computational time, which makes it suitable for analyses needing a balance between accuracy and efficiency.
- The S4R element offers similar accuracy to the S4 element, with slightly higher errors of 7.025% for axial compression, 4.868% for major axis bending, and 3.861% for minor axis bending, while significantly reducing computational time, enhancing overall efficiency and making it preferable for time-sensitive studies.
- The S4R5 element shows higher errors across all loading conditions, including 7.238% for axial compression and 4.102% for minor axis bending, and requires more computational time, limiting its suitability for routine applications.
- The S8R element produces competitive results with error percentages of 6.697% for axial compression, 3.319% for major axis bending, and 3.491% for minor axis bending, but demands significantly longer computational time.
- The S8R5 element achieves the highest accuracy with errors of 2.644% in major axis bending and 3.301% in minor axis bending but incurs substantial computational time and may yield unreliable results for buckling problems due to its internal node configuration.

- The S4R element is ideal for scenarios prioritizing computational efficiency while maintaining satisfactory accuracy.
- The S8R5 element is suitable for applications requiring slightly higher precision.
- Selecting an element type should involve a careful assessment of the trade-offs between computational demand and the required accuracy for the analysis.

REFERENCES

1. Gardner L, Fieber A, Macorini L (2019) Formulae for Calculating Elastic Local Buckling Stresses of Full Structural Cross-sections. Structures 17:2–20. https://doi.org/10.1016/j.istruc.2019.01.012
2. Nuraliyev M, Dundar MA, Sahin DE (2022) Determination of optimal dimensions of polymer-based rectangular hollow sections based on both adequate-strength and local buckling criteria: Analytical and numerical studies. Mech Based Des Struct Mach 1–31. https://doi.org/10.1080/15397734.2022.2139720
3. Singh TG, Chan T-M (2021) Effect of access openings on the buckling performance of square hollow section module stub columns. J Constr Steel Res 177:106438. https://doi.org/10.1016/j.jcsr.2020.106438
4. Hämäläinen O-P, Halme T, Björk T (2018) Local Buckling of Welded Box Beams Made of Ultrahigh-Strength Steels. J Struct Eng 144(7), 6018003.
5. Dundar MA, Nuraliyev M (2024) Parametric study on the assessment of the local buckling behavior of perforated square hollow sections with non-uniform wall thickness under axial compression TT - Düzgün olmayan duvar kalınlığına sahip delikli kare içi boş profillerin eksenel basınç alt. J Innov Eng Nat Sci 4(2):326–353. https://doi.org/10.61112/jiens.1397391
6. Shahbazian A, Wang YC (2011) Calculating the global buckling resistance of thin-walled steel members with uniform and non-uniform elevated temperatures under axial compression. Thin-Walled Struct 49(11):1415–1428. https://doi.org/https://doi.org/10.1016/j.tws.2011.07.001
7. Shahbazian A, Wang YC (2011) Application of the Direct Strength Method to local buckling resistance of thin-walled steel members with non-uniform elevated temperatures under axial compression. Thin-Walled Struct 49(12):1573–1583.
8. Yang D, Hancock GJ (2006) Numerical simulation of high-strength steel box-shaped columns failing in local and overall buckling modes. J Struct Eng 132(4):541–549.
9. Shen J, Wadee MA, Sadowski AJ (2017) Interactive buckling in long thin-walled rectangular hollow section struts. Int J Non Linear Mech 89:43–58. https://doi.org/10.1016/j.ijnonlinmec.2016.11.007
10. McCann F, Fang C, Gardner L, Silvestre N (2016) Local buckling and ultimate strength of slender elliptical hollow sections in compression. Eng Struct 111:104–118.
11. Thai H-T, Uy B, Khan M (2015) A modified stress-strain model accounting for the local buckling of thin-walled stub columns under axial compression. J Constr Steel Res 111:57–69.
12. Yu C, Schafer BW (2007) Simulation of cold-formed steel beams in local and distortional buckling with applications to the direct strength method. J Constr Steel Res 63(5):581–590.
13. Dai Y, Roy K, Fang Z, Chen B, Raftery GM, Lim JBP (2024) Buckling resistance of axially loaded cold-formed steel built-up stiffened box sections through experimental testing and finite element analysis. Eng Struct 302:117379. https://doi.org/10.1016/j.engstruct.2023.117379
14. DUNDAR MA, Nuraliyev M, Sahin DE (2022) Determination of Optimal Dimensions of Polymer-Based Rectangular Hollow Sections Based on Both Adequate-Strength and Local Buckling Criteria: Analytical and Numerical Study. Mech Based Des Struct Mach. https://doi.org/10.1080/15397734.2022.2139720
15. Liu M, Zhang L, Wang P, Chang Y (2015) Buckling behaviors of section aluminum alloy columns under axial compression. Eng Struct 95:127–137.
16. Paul B, Roy K, Lim JBP, Fang Z, McCollum K, Bell D (2023) Moment-capacity of bolted side-plates for apex joint of nested tapered box beam portal frames. J Build Eng 76:107011. https://doi.org/10.1016/j.jobe.2023.107011
17. Ozenc O, Dundar MA, Sahin DE (2023) Examination of compressive and flexural behaviors of acrylonitrile-butadiene-styrene filled with hemp fiber particles. J Thermoplast Compos Mater 37(2):743–771. https://doi.org/10.1177/08927057231186326
18. Gunalan S, Heva YB, Mahendran M (2015) Local buckling studies of cold-formed steel compression members at elevated temperatures. J Constr Steel Res 108:31–45.
19. Systèmes D (2014) ABAQUS Documentation (Dassault Systèmes, Providence, RI)

20. Hughes OF, Ghosh B, Chen Y (2004) Improved prediction of simultaneous local and overall buckling of stiffened panels. Thin-Walled Struct 42(6):827–856. https://doi.org/10.1016/j.tws.2004.01.003
21. Sadowski AJ, Rotter MJ (2013) On the relationship between mesh and stress field orientations in linear stability analyses of thin plates and shells. Finite Elem Anal Des 73:42–54. https://doi.org/10.1016/j.finel.2013.05.004
22. Anapayan T, Mahendran M (2012) Improved design rules for hollow flange sections subject to lateral distortional buckling. Thin-Walled Struct 50(1):128–140. https://doi.org/10.1016/j.tws.2011.09.004
23. Elglaad S, Elghandour M, Sharaf T, Elsabbagh A (2021) Assessment of the Finite Element Analysis of Portal Steel Frames with Cold Formed Rectangular Hollow Sections Including Imperfections and Residual Stresses. Port-Said Eng Res J 25(2):60–79.
24. Ozyurt E, Wang YC (2018) Resistance of Axially Loaded T- and X-Joints of Elliptical Hollow Sections at Elevated Temperatures – A Finite Element Study. Structures 14:15–31. https://doi.org/10.1016/j.istruc.2018.01.004
25. Grilo LF, Fakury RH, Rodrigues FC, Daldegan VP (2018) Behavior and design of built-up compressed steel members composed of concentric hot rolled circular hollow sections. Lat Am J Solids Struct 15:e51.
26. Mahmoud A, Torabian S, Jay A, Myers A, Smith E, Schafer BW (2015) Modeling protocols for elastic buckling and collapse analysis of spirally welded circular hollow thin-walled sections. Struct Stab Res Counc, AISC (American Institute of Steel Construction), Nashville, TN, USA, March 24-27, 1-16. https://doi.org/10.13140/2.1.4893.7763
27. Shariati M, Saemi J, Sedighi, M, Eipakchi HR (2011) Experimental and numerical studies on buckling and post-buckling behavior of cylindrical panels subjected to compressive axial load. Strength Mater 43:190–200. https://doi.org/10.1007/s11223-011-9285-x
28. Rokilan M, Mahendran M (2021) Design of cold-formed steel columns subject to local buckling at elevated temperatures. J Constr Steel Res 179:106539.
29. Wadee MA, Bai L (2014) Cellular buckling in I-section struts. Thin-Walled Struct 81:89–100.
30. Wadee MA, Farsi M (2014) Local–global mode interaction in stringer-stiffened plates. Thin-Walled Struct 85:419–430. https://doi.org/10.1016/j.tws.2014.09.012
31. Yuan HX, Wang YQ, Gardner L, Shi YJ (2014) Local–overall interactive buckling of welded stainless steel box section compression members. Eng Struct 67:62–76. https://doi.org/10.1016/j.engstruct.2014.02.012
32. Saliba N, Gardner L (2013) Experimental study of the shear response of lean duplex stainless steel plate girders. Eng Struct 46:375–391.
33. Zhou F, Young B (2013) Web crippling behaviour of cold-formed duplex stainless steel tubular sections at elevated temperatures. Eng Struct 57:51–62.
34. Hassanein MF (2010) Imperfection analysis of austenitic stainless steel plate girders failing by shear. Eng Struct 32(3):704–713.
35. Siahaan R, Keerthan P, Mahendran M (2016) Finite element modeling of rivet fastened rectangular hollow flange channel beams subject to local buckling. Eng Struct 126:311–327.
36. Becque J, Rasmussen KJR (2008) Numerical investigation and design methods for stainless steel columns failing by interaction of local and overall buckling, Research Report R888, School of Civil Engineering, University of Sydney.
37. Killpack M, Abed-Meraim F (2011) Limit-point buckling analyses using solid, shell and solid-shell elements. J Mech Sci Technol 25:1105–1117.
38. Nuraliyev M, Dundar MA, Akyildiz HK (2024) A novel analytical method for local buckling check of box sections with unequal wall thicknesses subjected to bending. Mech Adv Mater Struct 1–24. https://doi.org/10.1080/15376494.2024.2369262
39. Vieira L (2018) On the local buckling of RHS members under axial force and biaxial bending. Thin-Walled Struct 129:10–19. https://doi.org/10.1016/j.tws.2018.03.022
40. Seif M, Schafer BW (2010) Local buckling of structural steel shapes. J Constr Steel Res 66(10):1232–1247. https://doi.org/10.1016/j.jcsr.2010.03.015
41. Kroll WD, Fisher GP, Heimerl GJ (1943) Charts for calculation of the critical stress for local instability of columns with I-, Z-, channel, and rectangular-tube section. National Advisory Committee for Aeronautics. Report Number: NACA-WR-L-429
42. Radwan M, Kövesdi B (2021) Local plate buckling type imperfections for NSS and HSS welded box-section columns. Structures 34:2628–2643. https://doi.org/10.1016/j.istruc.2021.09.011
43. Möcker T, Linde P, Kraschin S, Goetz F, Marsolek J, Wohlers W (2008) Abaqus FEM Analysis of The Post Buckling Behaviour of Composite Shell Structures. Available at: https://www.researchgate.net/publication/267218447
44. Dassault Systèmes (2012) Abaqus Analysis User's Manual 6.12. http://orpheus.nchc.org.tw:2080/v6.12/. Accessed 02 Jan. 2025.

45. Ranawaka T, Mahendran M (2006) Finite element analyses of cold-formed steel columns subject to distortional buckling under simulated fire conditions. In: Proceedings of the International Colloquium on Stability and Ductility of Steel Structures. Instituto Superior Técnico, Lisbon, Portugal. pp 747–755.
46. Chandra KSS, Rao KV, Rajanna T (2020) Effect of Varying In-Plane Loads and Cutout Size on Buckling Behavior of Laminated Panels. In: Advances in Mechanical Engineering: Select Proceedings of ICAME 2020. Springer, pp 671–678.
47. El Bahaoui J, El Bakkali L, Khamlichi A (2012) Buckling strength of axially compressed thin axisymmetric shells as affected by localized initial geometric imperfections. Int Rev Appl Sci Eng 3(1):1–14.
48. Bin Kamarudin MN, Mohamed Ali JS, Aabid A, Ibrahim YE (2022) Buckling analysis of a thin-walled structure using finite element method and design of experiments. Aerospace 9(10):541:1-31. https://doi.org/10.3390/aerospace9100541
49. Lu W, Liu H, Waqas A, Long L (2023) Study on buckling behavior of multilayer pyramid lattice structures. Mech Adv Mater Struct 31(28):10059–10069. https://doi.org/10.1080/15376494.2023.2284271
50. Duarte APC, Pereira GB, Silvestre N (2021) Numerical study of the influence of the stringers cross-section geometry on the mechanical behavior of compressed curved stiffened composite panels. Mech Adv Mater Struct 28(5):516–529. https://doi.org/10.1080/15376494.2019.1578009
51. Ragheb WF (2010) Hybridization Effectiveness in Improving Local Buckling Capacity of Pultruded I-Beams. Mech Adv Mater Struct 17(6):448–457. https://doi.org/10.1080/15376494.2010.483328
52. Zhu J, Li L-Y (2019) Effect of shear stress on distortional buckling of CFS beams subjected to uniformly distributed transverse loading. Mech Adv Mater Struct 26(17):1423–1429. https://doi.org/10.1080/15376494.2018.1432798
53. Masood SN, Gaddikeri KM, Viswamurthy SR (2021) Experimental and finite element numerical studies on the post-buckling behavior of composite stiffened panels. Mech Adv Mater Struct 28(16):1677–1690. https://doi.org/10.1080/15376494.2019.1701151
54. Zhao W, Xie Z, Wang X, Li X, Hao J (2019) Buckling behavior of stiffened composite panels with variable thickness skin under compression. Mech Adv Mater Struct 26(3):215–223. https://doi.org/10.1080/15376494.2018.1495795